Lawrence Berkeley National Laboratory

Title
The mechanism of twin thickening and the elastic strain state of TWIP steel nanotwins

Permalink
https://escholarship.org/uc/item/01c5s81t

Authors
Kwok, TWJ
McAuliffe, TP
Ackerman, AK
et al.

Publication Date
2023-05-01

DOI
10.1016/j.msea.2023.145005

Peer reviewed
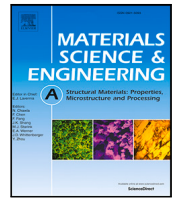
The mechanism of twin thickening and the elastic strain state of TWIP steel nanotwins

T.W.J. Kwok [a], T.P. McAuliffe [a], A.K. Ackerman [a], B.H. Savitzky [b], M. Danaie [c], C. Ophus [b], D. Dye [a,*]

[a] *Department of Materials, Royal School of Mines, Imperial College London, Prince Consort Road, London, UK*
[b] *National Center for Electron Microscopy (NCEM), Molecular Foundry, Lawrence Berkeley Lab, USA*
[c] *Electron Physical Science Imaging Centre (ePSIC), Diamond Light Source, Oxford, UK*

ARTICLE INFO

ABSTRACT

A Twinning Induced Plasticity (TWIP) steel with a nominal composition of Fe-16.4Mn-0.9C-0.5Si-0.05Nb-0.05V was deformed to an engineering strain of 6%. The strain around the deformation twins were mapped using the 4D-STEM technique. Strain mapping showed a large average elastic strain of approximately 6% in the directions parallel and perpendicular to the twinning direction. However, the large average strain comprised of several hot spots of even larger strains of up to 12%. These hot spots could be attributed to a high density of sessile Frank dislocations on the twin boundary and correspond to shear stresses of 1–1.5 GPa. The strain and therefore stress fields are significantly larger than other materials known to twin and are speculated to be responsible for the early thickness saturation of TWIP steel nanotwins. The ability to keep twins extremely thin helps improve grain fragmentation, *i.e.* the dynamic Hall–Petch effect, and underpins the large elongations and strain hardening rates in TWIP steels.

1. Introduction

Twinning has become increasingly significant in modern metallurgy [1]. Deformation or mechanical twinning occurs when a region of the crystal is sheared, with each atom moving less than one lattice spacing, such that the twinned region forms a mirror image of the parent crystal about the twinning or habit plane [2]. Many modern materials such as TWIP steels [3,4], medium Mn steels [5], TWIP Ti [6,7], Mg alloys and Zr alloys [8] all capitalise on twinning to enable high strain hardening rates and improve elongation. However, as Qin and Bhadeshia [9] point out, the maximum contribution of twinning to total elongation (true strain) in a random polycrystal is < 0.3. This is compared to total elongation of 0.5–0.6 true strain in TWIP steels [10,11]. It is therefore the interaction between twins and dislocations which are of importance. In TWIP steels, long and thin twins are formed during deformation, acting as barriers to dislocation motion. The volume fraction of twins increase with increasing strain and continuously subdivides the grain, resulting in a high strain hardening rate and also elongation. This mechanism has been termed the dynamic Hall–Petch effect [12,13].

In the case of Face Centred Cubic (FCC) crystals, the origin of twinning is still a matter of academic debate with many different mechanisms being proposed although the three layer twin nucleus model by Mahajan and Chin [15] is increasingly being used in computational models [10,16]. Nevertheless, the fundamentals of FCC twinning are well understood and first involves the dissociation of a full $\frac{a}{2}\{111\}\langle110\rangle$ into two $\frac{a}{6}\{111\}\langle112\rangle$ Shockley partial dislocations, where a is the FCC lattice spacing. In TWIP steels, the formation of partial dislocations is favoured due to the low Stacking Fault Energy (SFE). An FCC twin is then created, as shown in Fig. 1, when partial dislocations propagate on successive $\{111\}$ planes and increasing the twin thickness.

In TWIP steels, the deformation twins are often between 20−30 nm in thickness, corresponding to the glide of approximately 100 partial dislocations [10]. Interestingly, these twins generally do not continue to thicken with strain once this thickness is reached, rather choosing to form new twins instead. This is compared to a larger twin thickness of ≤ 100 nm in Cu–Al alloys [17] and 1–2 μm in α-brass [18]. Therefore, while there is a general mechanism for twin thickening, there also appears to be mechanism for twin thickness saturation based on some material property such as SFE [17] and grain size [19,20]. Unfortunately, the reasons for twin thickness saturation are not very well studied, even though the ability of TWIP steels to form a high density of very fine twins is paramount to a high degree of grain fragmentation, underpinning the dynamic Hall–Petch effect and overall tensile properties.
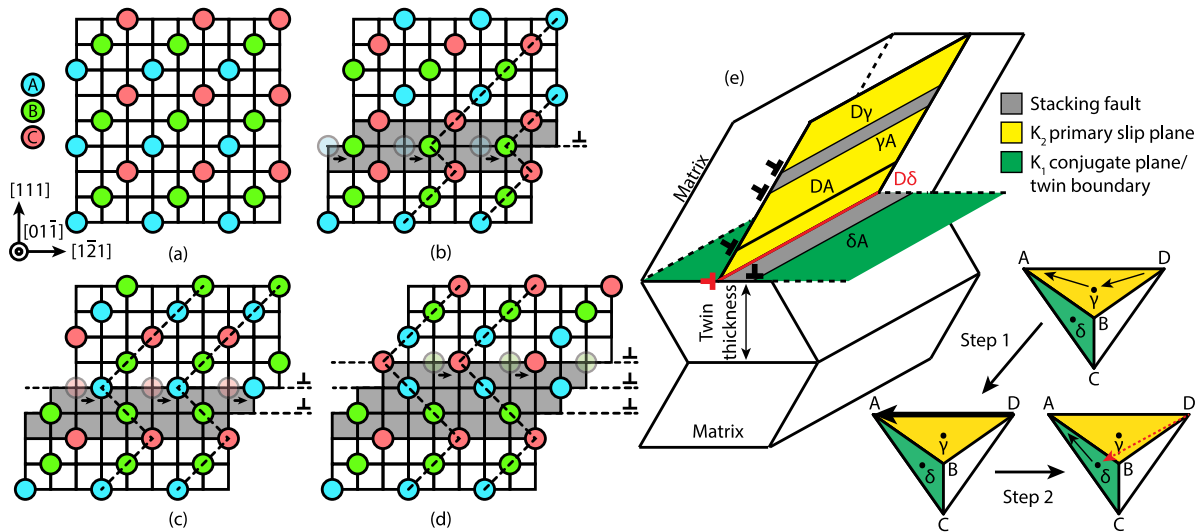

Fig. 1. Schematic ball and stick model of twinning in FCC materials. (a) Perfect FCC lattice with ABCABC stacking. (b) Passage of one, (c) two and (d) three Shockley partial dislocations on successive (111) planes building up the twin thickness. Grey regions indicate the growing twin. (e) Schematic of the interaction between dislocation and twin boundaries described by Idrissi and Schryvers [14], drawn after De Cooman et al. [10].

Nevertheless, Idrissi and Schryvers [14] studied the interaction between coherent twin boundaries and dislocations and proposed a "pole + deviation" mechanism that might help to control twin thickness. Illustrated in Fig. 1e, the first step involves two Shockley partials (Dγ and γA) gliding on the K_1 primary slip plane which constrict and recombine under applied stress to form a full dislocation (DA). In the second step, the full dislocation meets the coherent twin boundary and dissociates again under stress into a sessile Frank partial dislocation (Dδ) and a Shockley partial dislocation (δA) according to the reaction:

$$\frac{a}{2}\langle 110 \rangle \rightarrow \frac{a}{3}\langle 111 \rangle_{sessile} + \frac{a}{6}\langle 11\bar{2} \rangle \tag{1}$$

where the sessile Frank partial dislocation (Dδ) remains along the twin boundary and the Shockley partial dislocation (δA) glides off on the K_2 conjugate plane, increasing the twin thickness by one layer. Idrissi and Schryvers [14] then propose that the high density of sessile Frank partials on the twin boundary will affect the mobility of Shockley partials on the twinning plane (K_1), limiting the thickening of the twin. Recent computational work by Grilli et al. [21] confirmed the observations by Idrissi and Schryvers [14] that residual dislocations on the twin boundary can completely stop twin thickening and add that materials with a larger SFE produces larger twins.

To further investigate the reasons behind the early twin thickness saturation in TWIP steels, Four Dimensional Scanning Transmission Electron Microscopy (4D-STEM) can used to map the strain state in and around a mechanical twin. 4D-STEM is a relatively new technique where an electron diffraction pattern is acquired at every point in a scan grid where sub-nm spatial resolution can be achieved [22]. The term "4D" refers to the collection of 2D diffraction patterns over a 2D grid. A comprehensive review of 4D-STEM and its applications in strain mapping, imaging and ptychography is available in a review by Ophus [22].

2. Experimental

In this study, a 400 g ingot of steel with nominal composition of Fe-16.4Mn-0.9C-0.5Si-0.05Nb-0.05V (SFE $\approx$ 23 mJ m^{-2} [23]) based on the composition by Scott et al. [24] was produced by arc melting pure elements in a vacuum arc melter. The steel was cast into a copper crucible and homogenised at 1300 °C for 24 h in Ar. The steel ingot was then hot rolled from $10 \rightarrow 5$ mm (50% reduction) in 2 passes at 1000 °C, cold rolled from $5 \rightarrow 1.5$ mm (67% reduction) and finally annealed at 1000 °C for 5 min. Sub-sized tensile samples with gauge

dimensions of $19 \times 1.5 \times 1.5$ mm were obtained from the rolled strip *via* electrical discharge machining. Tensile samples were then tested to 6% engineering strain (approximately 5% plastic strain) and to failure, both at a nominal strain rate of 10^{-3} s^{-1}.

Electron Backscattered Diffraction (EBSD) was conducted using a Sigma 300 FEG-SEM on the as-annealed and 6% strained conditions. A strain of 6% was chosen to produce a sufficient twin density in order to locate the twins using EBSD while keeping background dislocation density to a minimum. In the 6% strained sample, a grain with a $\langle 111 \rangle$ crystallographic direction in the vertical axis of the microscope field of view was selected and a thin foil was extracted using the Focussed Ion Beam (FIB) lift-out technique, producing a foil with its $\langle 111 \rangle$ direction parallel to the foil normal.

4D-STEM and High Resolution Transmission Electron Microscopy (HR-TEM) was performed on the foil using the probe corrected JEOL ARM200CF Transmission Electron Microscope (TEM) at ePSIC (Oxford, United Kingdom). Diffraction patterns were collected with a Merlin (MediPix) direct electron detector. An accelerating voltage of 200 kV and a camera length of 40 cm were employed with a 10 µm CL1 aperture. A 68.2×83.1 nm area of interest was scanned in 188×229 real space pixels and with a 256×256 pixel diffraction pattern captured at each of these scan positions with a 1 ms dwell time per pattern.

The in-plane elastic strain was calculated from the electron diffraction pattern at each scan location. Bragg peak identification, dataset calibration including elliptical distortion correction and diffraction shift correction and elastic strain calculation were performed with the open source py4DSTEM analysis package [25]. For locating Bragg peaks, a correlation power of 1 was used, corresponding to cross-correlation [26], and achieve subpixel precision with local Fourier up-sampling by a factor of 16 [27]. For the rest of the paper, an orthogonal frame of reference with directions *1, 2, 3* will be adopted, where *3* refers to the [111] direction perpendicular to the surface of the foil, *1* as [1$\bar{2}$1] and *2* as [10$\bar{1}$].

To highlight deviation from perfect crystal symmetry, centre of symmetry analysis was applied to HR-TEM data obtained from the same foil. To achieve this, pattern spot masking was applied to the Fast Fourier Transformed (FFT) pattern using the Gatan Digital Micrograph software. This image was then further refined by filtering *via* a MATLAB script using Lucy-Richardson deblurring a Gaussian Point Spread Function (PSF) reconvolution. The nearest neighbours could then be calculated for each column and the local crystal symmetry analysed to highlight defects within the matrix. Therefore, a centre
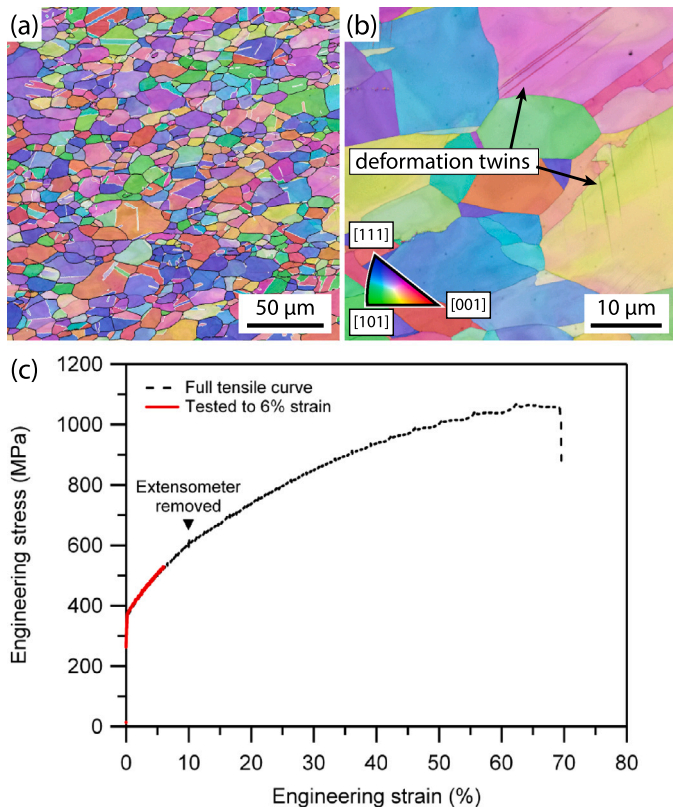
Fig. 2. EBSD IPF-X (right) and image quality maps of (a) as-annealed sample where black lines indicate high angle grain boundaries and white lines indicate austenite $\Sigma3$ boundaries (rolling direction parallel to the horizontal axis and transverse direction pointing out of the page), (b) sample deformed to 6% strain, demonstrating fine deformation twins. (c) Engineering tensile curves of the investigated steel when tested to failure and to 6% strain.

of symmetry parameter, M_i, can be calculated and is given by the following equation:

$$M_i = \frac{\frac{1}{2} \times \sum_{r=1}^{6} D_r}{2 \times \sum_{r=1}^{6} |d_r|^2}$$ (2)

where the 6 nearest neighbours to a central atomic column, i, are given a rank r according to their distance from the atom. The coordinates were then calculated, giving a position vector d_r. For every d_r, the remaining nearest neighbours are searched to find the smallest D_r, where $D = |d_i + d_j|^2$. In the event of a perfect lattice, d_i and d_j will be on opposite corners, resulting in a D which equals to 0. Therefore, M_i can be visualised as a qualitative measure of deviation from a perfect lattice based on the arrangement of atomic columns. A false colour map could then be generated to highlight deviations from perfect crystal symmetry as a result of defects such as dislocations and strain within the crystal matrix. Eq. (2) was originally established by Kelchner et al. [28] and adapted by Ackerman et al. [29]

3. Results and analysis

The microstructure of the as-annealed TWIP steel is shown in Fig. 2a with an area weighted average grain size of 12 μm. An EBSD map of the 6% strained sample is shown in Fig. 2b. Unfortunately, due to the fine twin thickness, it is not easy to index deformation twins using EBSD. However, they can be identified as darker lines in the Image Quality (IQ) map. The tensile behaviour of the investigated steel is shown in Fig. 2c and has a yield strength of 360 MPa, tensile strength of 1050 MPa and total elongation of 69%.

Fig. 3a–d shows the Virtual Bright and Dark Field (VBF and VDF respectively) images reconstructed from the intensity collected from the highlighted digital apertures. VBF images in Fig. 3a–b clearly distinguish the twin from the matrix. Given the axis system we have adopted with [111] out of the plane and the diffraction vectors indexed in Fig. 3e, it is inferred that the twins have a habit plane of $(11\bar{1})$.

In conventional TEM, the direct beam contains a large amount of structure-dependent information. Conventional bright field imaging when used with an objective aperture to isolate the direct beam, uses electron wave phase information as well as intensity to re-interfere and reconstruct an image [30]. In VBF, only access to electron intensity in the diffraction plane is available. Therefore it is likely that the observed contrast between twin and matrix is derived from local strain, lattice rotation or dynamical effects which will alter the ratio of diffracted to direct intensity. The high angle VDF image in Fig. 3c is similar to convention High-Angle Annular Dark Field (HAADF) imaging which detects electrons which are scattered to high angles and also suggests that there was no detectable variation in local chemistry between the twin and the matrix. The twin is explicitly highlighted in Fig. 3d by reconstructing the spatial image from the $00\bar{2}$ reciprocal lattice point for the twinned region only, similar to a conventional TEM dark field image. The action of twinning rotates the diffraction pattern about the direct beam, such that the twinned and untwinned $02\bar{2}$ peaks are separated. In Fig. 3e, a Bragg vector map is presented (after Savitzky et al. [25]), showing the distribution of all measured Bragg peak locations for the untwinned region. It is acknowledged that a small amount of intensity is observed at the twin reciprocal lattice points even for the untwinned material. This is possibly due to the geometry of the sample, *i.e.* twinning habit plane not perfectly parallel to beam direction, and through thickness sampling of both untwinned and twinned material near the interface.

The strain components $\varepsilon_{11}, \varepsilon_{22}, \varepsilon_{12}$ were calculated from the relative movements of the diffraction spots. This operation was performed independently for twinned and untwinned regions. A set of reference reciprocal lattice vectors were obtained by averaging the untwinned regions's reciprocal lattice basis vectors. The magnitude of the twin basis vectors were normalised to this unstrained length. As such, elastic strains are given with reference to this "unstrained" state. The measurement could alternatively be considered as the elastic strain variation across the area of interest.

Maps of the measured (11, 22, 12) and inferred strain components across the area of interest are shown in Fig. 4. An average line profile in the 1-direction was obtained by integrating points along the 2-direction within the highlighted area. From the average profiles in Fig. 4, it is striking that the average elastic strains in the 11 and 22 directions reach values as high as 6% at locations along the twin boundaries. Hot spots of up to 12% were also observed at certain points along the twin boundaries. These values far exceed other elastic strain measurements observed in the literature (Table 1), even between other 4D-STEM experiments with the same methodology, *e.g.* ∼ 4% observed by Pekin et al. along twin boundaries in stainless steel 304 [26]. However, it should be noted that the averaged strains have been disproportionately raised above the baseline of approximately 4% by the presence of hot spots.

HR-TEM centre of symmetry analysis was conducted on another region from the same foil and the results are shown in Fig. 5. The Bright Field (BF) micrograph in Fig. 5a shows three twin boundaries. It is likely that TB1 and TB2 enclose a very thin twin while TB3 is the right hand boundary of a thicker twin. In order to analyse the apparent interfacial strain qualitatively, the crystal symmetry of the atomic columns was calculated as shown by the cleaned High Angle Annular Dark Field (HAADF) micrograph in Fig. 5b and plotted in Fig. 5c. From Fig. 5c, it can be seen that the significant deviations from the perfect lattice were found along all three TBs. Although centre of symmetry analysis is qualitative, it confirms the presence of strain hot spots along twin boundaries as shown by 4D-STEM in Fig. 4.
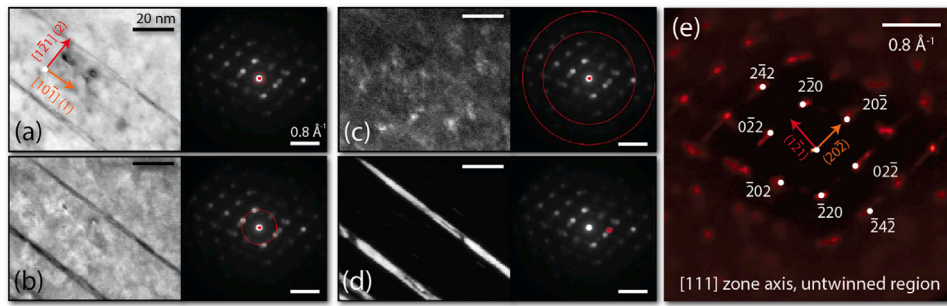
Fig. 3. (a,b) Virtual bright and (c,d) dark field images of the steel nanotwin using different virtual apertures indicated by the open red circles. (e) Average deconvolution maps, sums over real space of the identified Bragg peak locations weighted by intensity.
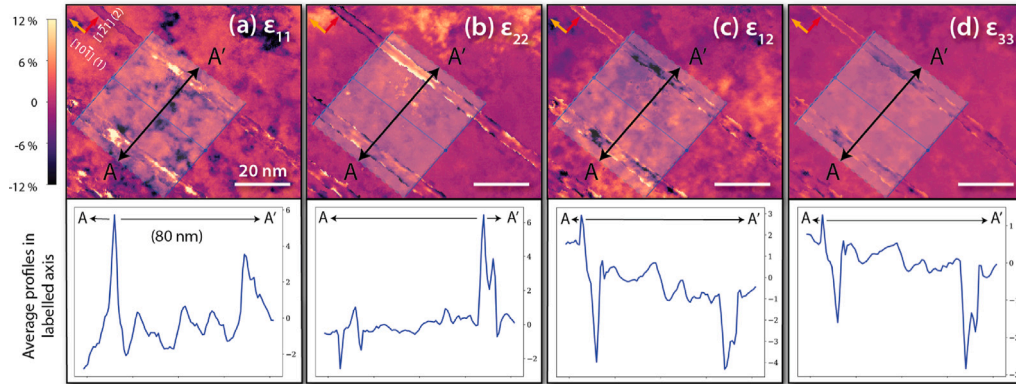

Fig. 4. Elastic strain maps resolved in the (a) 11, (b) 22, (c) 12 and (d) 33 directions. The average 1-direction profile, perpendicular to the twin's length, was calculated by integrating all points along the *2*-direction within the highlighted region.
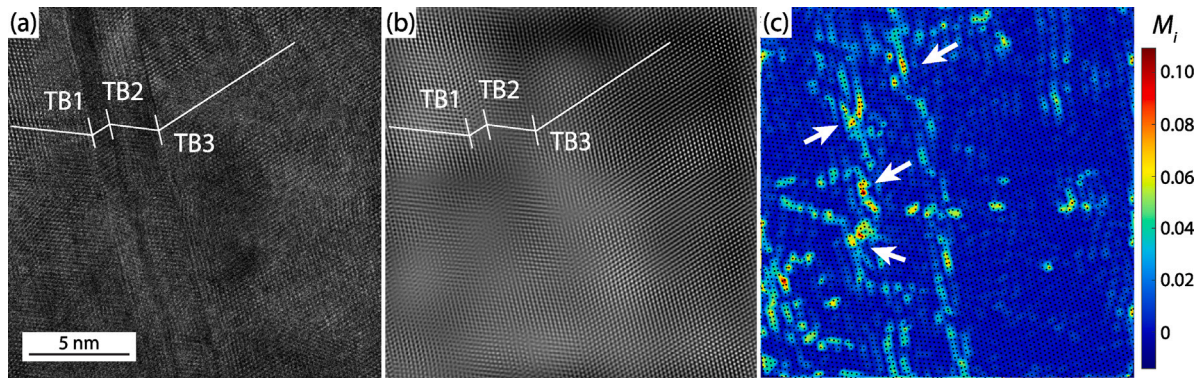

Fig. 5. (a) HR-TEM BF micrograph of three Twin Boundaries (TB) labelled 1–3. (b) HAADF micrograph with pattern spot masking applied to filter out noise in the FFT. (c) Centre of symmetry analysis highlighting deviation from perfect crystal symmetry along the twin boundaries. Arrows pointing to regions of high distortion of the crystal lattice along all three TBs. Beam direction was parallel to the [110] direction.

Table 1
Comparison of strain, ε, in % obtained with different strain mapping methods on various materials. *SS—Stainless Steel, CP—Commercially Pure, N-PED—Nano-Precession Electron Diffraction.

Material	Method	Feature	ε	Reference
AISI 321 (SS)	4D-STEM	Planar dislocations	0.5	[31]
Boron Carbide	N-PED	Grain boundary	0.75	[32]
Pd	HR-TEM	Twins	2.5	[33]
SS 304	4D-STEM	Twins	4	[26]
CP Mg	4D-STEM	Twins	4	[34]
TWIP steel	4D-STEM	Twins	6	Current

4. Discussion

The presence of hot spots was also observed by Rösner et al. [33] in a cold rolled Pd foil. These hot spots of approximately $\leq 25\%$ strain were attributed to dislocation debris when mapping the strain of dislocation cores of stacking faults or partial dislocations in the foil. It should therefore also follow, that the hot spots observed at the twin boundaries in Fig. 4 were the result of a highly dislocated structure. Following the "pole + deviation" mechanism proposed by Idrissi and Schryvers [14], the hot spots are likely to be the locations where one slip system impinges onto the twin boundary, generating a high density of sessile Frank partial dislocations at the twin boundary and also generating a very large stress field. Faulted twin boundaries as a result of impingement from another slip system were also shown by

Dao et al. [35] in nanotwinned Cu using HR-TEM. Furthermore, since the sample was only deformed to 5% strain, it is likely that only a few slip systems would have been activated, hence the localisation of strain only at certain points along the entire twin boundary.

In the study by Grilli et al. [21], it was found that an additional shear stress of 400 MPa to the critical resolved shear stress for twinning in α-uranium (orthorhombic) was sufficient to completely retard twinning and favour slip instead. Using the analytical model from Müllner et al. [36–38], it was estimated that the strain hot spots at the twin boundaries in the investigated steel resulted in a shear stress of approximately 1–1.5 GPa [39] (shear modulus of austenite being 65 GPa [12]), significantly larger than the shear stress needed to retard twinning in α-uranium. This large shear stress may help to explain why deformation twins in TWIP steels remain very thin.

However, it should be noted that the twins imaged in the current sample were only 4 nm thick, whereas the "saturation" twin thickness in TWIP steels is approximately 30 nm [10], suggesting that these twins will continue to thicken with increasing strain. Based on the conclusions by Grilli et al. [21] that twin growth is stopped when a critical density of residual dislocations on the twin boundary is reached, it is speculated that by the time the twin has grown to approximately 30 nm, the strain field along the twin boundary would have become more uniform, *i.e.* no more hot spots. The high density of dislocations along the twin boundary would then be able to completely stop the motion of Shockley partial dislocations along the twin boundary and the twin would then reach its maximum thickness.

The existence of hot spots may also help to explain the variability of twin thickness. De Cooman et al. [10] showed that while twins are commonly considered to be plate-like in morphology, TEM observations have shown twin thicknesses to be highly variable and twin boundaries to be highly faulted [35]. The formation of faulted twin boundaries appear to be caused by the disorderly overlapping of Shockley partial dislocations [10]. Therefore, it is speculated that while the hot spots may not have been sufficient to completely stop twin thickening at early strains, they will certainly disrupt the propagation of Shockley partials along the twin boundary leading to twin growth with irregular thicknesses.

5. Conclusion

In summary, the 4D-STEM and HR-TEM techniques were used to experimentally observe the strain fields in and around several deformation twins in a TWIP steel with sub-nm resolution. The results show several strain hot spots of up to 12% along the twin boundaries which very likely correspond to sessile Frank dislocations along the twin boundaries according to the "pole + deviation" mechanism proposed by Idrissi and Schryvers [14]. The observed average strain of 6% corresponds to a large shear stress of 1–1.5 GPa along the twin boundaries compared to other materials and is likely to be responsible for early retardation of twin growth and thickness saturation. This mechanism for twin thickness saturation helps to keep deformation twins in TWIP steels extremely fine, resulting in increased grain fragmentation with applied strain which is central to the dynamic Hall–Petch effect and underpins the impressive tensile properties of TWIP steels.

CRediT authorship contribution statement

T.W.J. Kwok: Methodology, Formal analysis, Writing – original draft, Writing – review & editing, Visualisation. **T.P. McAuliffe:** Methodology, Software, Validation, Formal analysis, Data curation, Writing – original draft, Writing – review & editing, Visualisation. **A.K. Ackerman:** Methodology, Validation, Formal analysis, Data curation, Writing – review & editing, Visualisation. **B.H. Savitzky:** Methodology, Software, Formal analysis, Data curation, Visualisation. **M. Danaie:** Methodology, Software, Formal analysis, Data curation. **C. Ophus:** Methodology, Software, Formal analysis, Data curation,

Writing – review & editing, Visualisation, Supervision, Funding acquisition. **D. Dye:** Conceptualisation, Methodology, Validation, Formal analysis, Writing – review & editing, Supervision, Funding acquisition.

Declaration of competing interest

The authors declare that they have no known competing financial interests or personal relationships that could have appeared to influence the work reported in this paper.

Data availability

Data will be made available on request.

Acknowledgements

References

[1] K. Lu, L. Lu, S. Suresh, Strengthening materials by engineering coherent internal boundaries at the nanoscale, Science 324 (5925) (2009) 349–352.

[2] A. Cottrell, An Introduction To Metallurgy, second ed., The Institute of Materials, London, 1995.

[3] K.M. Rahman, V.A. Vorontsov, D. Dye, The dynamic behaviour of a twinning induced plasticity steel, Mater. Sci. Eng. A 589 (2014) 252–261.

[4] K.M. Rahman, N.G. Jones, D. Dye, Micromechanics of twinning in a TWIP steel, Mater. Sci. Eng. A 635 (2015) 133–142.

[5] T.W.J. Kwok, P. Gong, R. Rose, D. Dye, The relative contributions of TWIP and TRIP to strength in fine grained medium-Mn steels, Mater. Sci. Eng. A 855 (2022) 143864.

[6] G.H. Zhao, X. Xu, D. Dye, P.E. Rivera-Díaz-del Castillo, Microstructural evolution and strain-hardening in TWIP Ti alloys, Acta Mater. 183 (2020) 155–164.

[7] J. Gao, Y. Huang, D. Guan, A.J. Knowles, L. Ma, D. Dye, W.M. Rainforth, Deformation mechanisms in a metastable beta titanium twinning induced plasticity alloy with high yield strength and high strain hardening rate, Acta Mater. 152 (2018) 301–314.

[8] H. Abdolv, A.J. Wilkinson, Assessment of residual stress fields at deformation twin tips and the surrounding environments, Acta Mater. 105 (2016) 219–231.

[9] B. Qin, H.K. Bhadeshia, Plastic strain due to twinning in austenitic TWIP steels, Mater. Sci. Technol. 24 (8) (2008) 969–973.

[10] B.C. De Cooman, Y. Estrin, S.K. Kim, Twinning-induced plasticity (TWIP) steels, Acta Mater. 142 (2018) 283–362.

[11] B.C. De Cooman, K.g. Chin, J. Kim, High Mn TWIP steels for automotive applications, in: M. Chiaberge (Ed.), New Trends and Developments in Automotive System Engineering, Chap. 6, IntechOpen, 2011, pp. 101–128.

[12] J.P. Allain S, O. Bouaziz, A physical model of the twinning-induced plasticity effect in a high manganese austenitic steel, Mater. Sci. Eng. A 387–389 (2004) 143–147.

[13] O. Bouaziz, N. Guelton, Modelling of TWIP effect on work-hardening, Mater. Sci. Eng. A 319-321 (2001) 246–249.

[14] H. Idrissi, D. Schryvers, Investigation of the elementary mechanisms controlling dislocation/twin boundary interactions in fcc metals and alloys: from conventional to advanced TEM characterization, in: A. Méndez-Vilas (Ed.), Current Microscopy Contributions To Advances in Science and Technology, Badajoz, Spain, 2012, pp. 1213–1224.

[15] S. Mahajan, G.Y. Chin, Formation of deformation Twins in F.C.C. crystals, Acta Metall. 21 (1973) 1353–1363.

[16] D.R. Steinmetz, T. Jäpel, B. Wietbrock, P. Eisenlohr, I. Gutierrez-Urrutia, A. Saeed-Akbari, T. Hickel, F. Roters, D. Raabe, Revealing the strain-hardening behavior of twinning-induced plasticity steels: Theory, simulations, experiments, Acta Mater. 61 (2) (2013) 494–510.

[17] Y. Zhang, N.R. Tao, K. Lu, Effect of stacking-fault energy on deformation twin thickness in Cu-Al alloys, Scr. Mater. 60 (4) (2009) 211–213.

[18] B. Roy, N.K. Kumar, P.M.G. Nambissan, J. Das, Evolution and interaction of twins, dislocations and stacking faults in rolled α-brass during nanostructuring at sub-zero temperature, AIP Adv. 4 (6) (2014).

[19] K.M. Rahman, V.A. Vorontsov, D. Dye, The effect of grain size on the twin initiation stress in a TWIP steel, Acta Mater. 89 (2015) 247–257.

[20] A. Ghaderi, M.R. Barnett, Sensitivity of deformation twinning to grain size in titanium and magnesium, Acta Mater. 59 (20) (2011) 7824–7839.

[21] N. Grilli, A.C. Cocks, E. Tarleton, A phase field model for the growth and characteristic thickness of deformation-induced twins, J. Mech. Phys. Solids 143 (2020).

[22] C. Ophus, Four-dimensional scanning transmission electron microscopy (4D-STEM): From scanning nanodiffraction to ptychography and beyond, Microsc. Microanal. (2019) 563–582.

[23] B. Sun, F. Fazeli, C. Scott, N. Brodusch, R. Gauvin, S. Yue, The influence of silicon additions on the deformation behavior of austenite-ferrite duplex medium manganese steels, Acta Mater. 148 (2018) 249–262.

[24] C. Scott, B. Remy, J.L. Collet, A. Cael, C. Bao, F. Danoix, B. Malard, C. Curfs, Precipitation strengthening in high manganese austenitic TWIP steels, Int. J. Mater. Res. 102 (5) (2011) 538–549.

[25] B.H. Savitzky, L. Hughes, K.C. Bustillo, H.D. Deng, N.L. Jin, E.G. Lomeli, W.C. Chueh, P. Herring, A. Minor, C. Ophus, py4DSTEM: Open source software for 4D-STEM data analysis, Microsc. Microanal. 25 (S2) (2019) 124–125.

[26] T.C. Pekin, C. Gammer, J. Ciston, A.M. Minor, C. Ophus, Optimizing disk registration algorithms for nanobeam electron diffraction strain mapping, Ultramicroscopy 176 (2017) 170–176.

[27] M. Guizar-Sicairos, S.T. Thurman, J.R. Fienup, Efficient subpixel image registration algorithms, Opt. Lett. 33 (2) (2008) 156.

[28] C.L. Kelchner, S.J. Plimpton, J.C. Hamilton, Dislocation nucleation and defect structure during surface indentation, Phys. Rev. B 58 (17) (1998) 11085–11088.

[29] A.K. Ackerman, V.A. Vorontsov, I. Bantounas, Y. Zheng, Y. Chang, T. McAuliffe, W.A. Clark, H.L. Fraser, B. Gault, D. Rugg, D. Dye, Interface characteristics in an $\alpha + \beta$ titanium alloy, Phys. Rev. Mater. 4 (1) (2020) 1–7.

[30] D.B. Williams, C.B. Carter, Transmission Electron Microscopy: A Textbook for Materials Science, second ed., Springer.

[31] T.C. Pekin, C. Gammer, J. Ciston, C. Ophus, A.M. Minor, In situ nanobeam electron diffraction strain mapping of planar slip in stainless steel, Scr. Mater. 146 (2018) 87–90.

[32] P.F. Rottmann, K.J. Hemker, Nanoscale elastic strain mapping of polycrystalline materials, Mater. Res. Lett. 6 (4) (2018) 249–254.

[33] H. Rösner, N. Boucharat, K.A. Padmanabhan, J. Markmann, G. Wilde, Strain mapping in a deformation-twinned nanocrystalline Pd grain, Acta Mater. 58 (7) (2010) 2610–2620.

[34] J.S. Chen, Y. Liu, R.J. McCabe, J. Wang, C.N. Tomé, Quantifying elastic strain near coherent twin interface in magnesium with nanometric resolution, Mater. Charact. 160 (2019) (2020) 110082.

[35] M. Dao, L. Lu, Y.F. Shen, S. Suresh, Strength, strain-rate sensitivity and ductility of copper with nanoscale twins, Acta Mater. 54 (20) (2006) 5421–5432.

[36] P. Müllner, C. Solenthaler, M.O. Speidel, Second order twinning in austenitic steel, Acta Metall. Mater. 42 (5) (1994) 1727–1732.

[37] P. Müllner, On the ductile to brittle transition in austenitic steel, Mater. Sci. Eng. A 234-236 (1997) 94–97.

[38] P. Müllner, C. Solenthaler, P.J. Uggowitzer, M.O. Speidel, Brittle fracture in austenitic steel, Acta Metall. Mater. 42 (7) (1994) 2211–2217.

[39] T. McAuliffe, A. Ackerman, B. Savitzky, T. Kwok, M. Danaie, C. Ophus, D. Dye, 4D-STEM elastic stress state characterisation of a TWIP steel nanotwin, 2020, arXiv:2004.03982v2.